RSC Advances

ROYAL SOCIETY OF CHEMISTRY

www.rsc.org/advances

RSC Advances

ARTICLE

Porous metallic nanocone arrays for high-density SERS hot spots via solvent-assisted nanoimprint lithography of block copolymer

Received 00th January 20xx,
Accepted 00th January 20xx

DOI: 10.1039/x0xx00000x

www.rsc.org/

Yunha Ryu,[a] Gumin Kang,[a] Chang-Won Lee*[b] and Kyoungsik Kim*[a]

Porous nanostructures have been enthusiastically investigated for SERS application thanks to the internal nanogaps or protrusions acting as effective electromagnetic hotspots. In this work, we report a facile fabrication method of highly porous metallic nanocone arrays for SERS application by integrating solvent-assisted nanoimprint lithography and selective etching of block copolymer (PS-b-PMMA) film. By taking advantage of the solvent-assisted nanoimprint, we easily mould the block copolymer film under atmospheric pressure and moderate temperature below the glass transition temperature in a short time. Then, PMMA domain of patterned block copolymer film was selectively etched to make porous structures to form dense nanogaps and protrusions. After Ag deposition, fabricated structure exhibited maximum enhancement factor (EF) up to ~3.5×10^6. In comparison to Ag coated "solid" nanocone arrays, the EF of "porous" nanocone arrays is maximum ~8.9 times enhanced, which demonstrates the effectiveness of the internal nanogaps and protrusions as plasmonic hot spots. Our fabrication method is very time-saving and cost-effective with good SERS enhancement and also can be easily applied to conventional SERS substrates or other applications that utilize porous structures.

1. Introduction

Raman spectroscopy is one of the most powerful tools for molecule detection or investigating the structural information of the chemicals. However, its low sensitivity due to the extremely small probability of the inelastic Raman scattering of light has hindered the widespread use of Raman spectroscopy in practical applications. Thus, Surface Enhanced Raman Scattering (SERS), a highly enhanced Raman scattering observed from the molecules adsorbing on the nanostructured metal surface, has been intensely studied since its discovery in 1970s.[1]

It has been known that there are two mechanisms of SERS; electromagnetic (EM) and chemical mechanism. The EM mechanism plays a major role in SERS phenomenon.[2] EM mechanism explains that SERS is induced from the strong electric field confinement as a result of localized surface plasmon resonance (LSPR) of metal nanostructures. The SERS enhancement factor (EF) from the EM mechanism is approximated by

$$\mathrm{EF} = |\mathrm{E}(\omega)|^2 |\mathrm{E}(\omega')|^2,$$

where $\mathrm{E} = E_{Loc}/E_{inc}$ (E_{Loc} : local electric field amplitude at the molecule position, E_{inc}: incident filed amplitude), ω is the incident frequency, and ω' is the Stokes-shifted frequency. Therefore, it is important to increase the density of electromagnetic hot spots to enhance the optical near field intensity. Various plasmonic nanostructures such as periodic metal arrays,[3-5] roughened metal surface,[6, 7] nanogap[8-10] have been investigated for SERS substrates for large near field enhancement.

One of the approaches to fabricate the structures with dense hot spots is using porous nano materials such as porous silicon,[11-13] anodic aluminum oxide (AAO),[14, 15] and nanoporous metal.[16-19] Internal pores or protrusions on a scale of tens of nanometers excites LSPR and thus can be strong EM hotspots. The pore size is tunable by controlling the fabrication conditions, so that LSPR response can be optimized with respect to the wavelength of the excitation light source. Moreover, due to the large surface area, porous structures can capture more target molecules than solid structures in a same detection area.

In this work, we demonstrate facile, time-saving and cost-effective fabrication method of porous nanostructured SERS substrate with dense electromagnetic hot spots by integrating soft nanoimprint lithography and selective etching of block copolymer (BCP). BCP is widely used to make nanoporous structures because selective etching of the microdomains of the BCP can generate nanostructures with high porosity.[20-23] We use Polystyrene-b-polymethyl methacrylate (PS-b-PMMA) BCP because PMMA domain can be selectively etched by simple process such as UV irradiation and wet etching in solvent, and the remaining PS domain turns into porous structure. And we apply the imprinting of the nanocone patterns into the BCP film to make SERS substrate with increased density of SERS hot spots and total surface area. Instead of previously used thermal

[a] School of Mechanical Engineering, Yonsei University, 50 Yonsei-ro, Seodaemun-gu, Seoul 120-749, Korea. E-mail: kks@yonsei.ac.kr
[b] Samsung Advanced Institute of Technology, Suwon, Korea. E-mail: cwlee42@gmail.com
* Corresponding authors

nanoimpint lithography,[24] we use solvent-assisted nanoimprint lithography (SAIL) to reduce the fabrication time and cost for patterning BCP film.[25, 26] By taking advantage of a solvent which dissolves both domain of the diblock copolymer, the BCP film could be easily moulded under the moderate temperature (<60 ℃) and atmospheric pressure in 20-30 minutes. After Ag deposition on the porous polymer structure, we measured Raman intensity for SERS application. By comparing SERS signals of Ag coated "porous" nanocone and "solid" nanocone, we find internal pores and protrusions of the porous structures play significant roles of effective SERS hot spots.

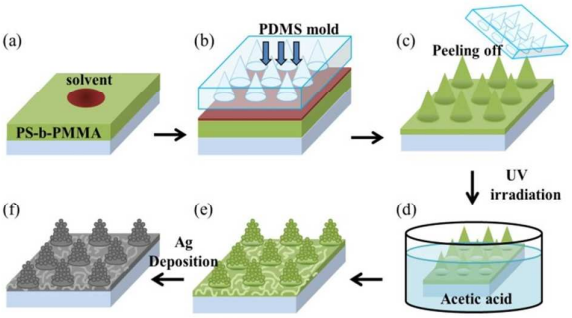

Fig. 1 The schematic of the fabrication process of porous metallic nanocone array

2. Experimental

2.1 Materials

Polystyrene-b-polymethyl methacrylate (PS-b-PMMA) diblock copolymer (Lot No.P718-SMMA, Polymer Source) with total molecular weight Mw of 94400 (MPS=45.9k and MPMMA=138k) and polydispersity index Mw/Mn=1.18 was purchased and used as received. The volume fraction of PS is 0.27 and the diameter of PS ligament is about 30~40 nm (See supplementary information Fig S2a). The diblock copolymer was dissolved in toluene sufficiently with a concentration of 2wt %.

2.2 Fabrication of Moulds

Nanocone-shaped Si master mould was fabricated by colloidal lithography and single-step deep reactive ion etching (SDRIE) process following the steps of our previous work.[27] Polystyrene (PS) nanospheres were self-assembled into hexagonally close-packed monolayer on air-water interface and transferred onto the hydrophilic-treated Si substrate. By using the PS nanosphere array as an etch mask, the Si substrate was etched by RIE to fabricate a nanocone array. Daughter mould for solvent-assisted nano-imprint lithography was made from a composite of hard poly(dimethylsiloxane) (h-PDMS) and soft PDMS (Sylgard® 184; Dow Corning). The composite stamp can replicate the shape of the master mould with higher accuracy compared with the soft PDMS mould.[28, 29]

2.3 Structural and Optical characterization

For structural characterization, the morphologies of the Ag coated nanocone (AgNC) and Ag coated porous nanocone (AgPNC) were observed by using scanning electron microscope (SEM, JSM-7001F, JEOL Ltd.) and a dual-beam Focused Ion Beam (FIB, FEI Nova 200 Nanolab) system combined with SEM. The total reflectance and transmittance spectra were obtained using a spectrophotometer (UV3600, Shimadzu Scientific Instruments) with an integrating sphere (MPC-3100) to investigate far-field optical properties of the samples.

2.4 SERS measurement

For Raman measurement, we used Rhodamine 6G (R6G) dye as a probe molecule. 10 µl of $10^{-5}M$ R6G ethanol solution was dropped onto the SERS substrates and dried at ambient conditions. Also, the same amount of $10^{-1}M$ R6G solution on glass was drop-casted to get reference Raman spectra. Measurement was carried out using a Raman spectrometer (LabRam Aramis, Horriba Jovin Yvon) with a microscope equipped with a 50×, NA 0.75 objective lens. For excitation sources, 532 nm ND:YAG laser (0.05 mW) and 633 nm He-Ne laser (0.17 mW) were used. Laser spot diameter can be calculated using $d = 1.22\lambda/NA$ under tightly focused conditions, which gives the diameter of 865 nm for 532 nm laser and 1030 nm for 633 nm laser. The accumulation time for the 532 nm and 633 nm laser excitation was 1 s and 5 s, respectively. All the Raman spectra were baseline corrected by the software (labspec, Horriba Jovin Yvon) with polynomial baseline fitting.

3. Results and Discussion

3.1 Fabrication process

The entire fabrication process of the porous metallic nanocone array is schematically shown in Figure 1. To fabricate nanocone array structure, we firstly patterned PS-b-PMMA BCP thin film via SAIL.[30] Because the solvent dissolves the resist layer, SAIL does not require high temperature or high pressure, and total fabrication time can be reduced. Then, PMMA domain was selective etched from BCP nanocone to make internal porosity. First, 2 wt% PS-b-PMMA block copolymer (BCP) solution in toluene was spin-coated on soda-lime glass with a rotating speed of 1000 rpm and left until the toluene is fully evaporated. Then, ~ 2 µl/cm^2 of acetone was dropped to an inverse-cone-shaped h-PDMS/PDMS composite mould. The composite mould was brought into conformal contact with the PS-b-PMMA coated glass substrate for 5 min at room temperature and 5 min at 60℃. Acetone is a good solvent both for the PS and PMMA polymer, thus PS-b-PMMA film is dissolved and conforms to the surface topology of the PDMS mould. As the acetone evaporates through the mould, block copolymer solidifies again and forms the cone shape. Then, PDMS mould was gently peeled off from the imprinted nanocone pattern. To show the quality of nanoimprint technique, scanning electron microscope (SEM) images of Si master mould and imprinted nanocones are presented in supplementary information, figure S1b. For selective etching of PMMA domain, PS-b-PMMA nanocone was irradiated with an ultraviolet lamp with a maximum intensity at 254 nm for 30 min and dipped in a 7:3 mixture of acetic acid and water for 30 min. SEM images of the porous nanocone structure after selective etching is presented in supplementary information Fig S2b. Finally, 30 nm-

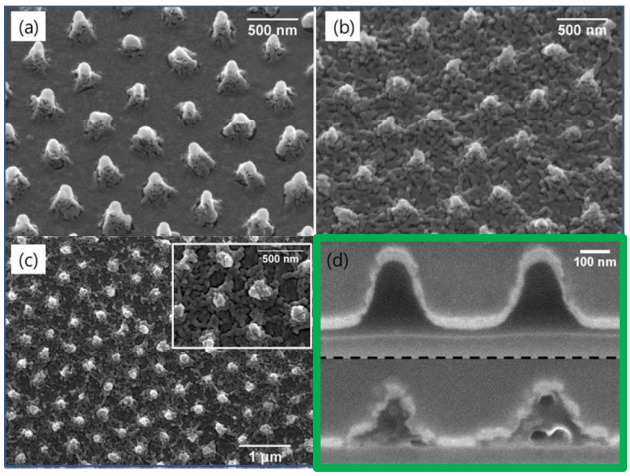

Fig. 2 SEM images of the Ag coated (a) nanocone (AgNC), (b) porous nanocone (AgPNC) array, 30°-tilt view, (c) normal images of AgPNC, (d) cross-section images of AgNC(upper) and AgPNC(lower) obtained using FIB-SEM with 52°-tilt view.

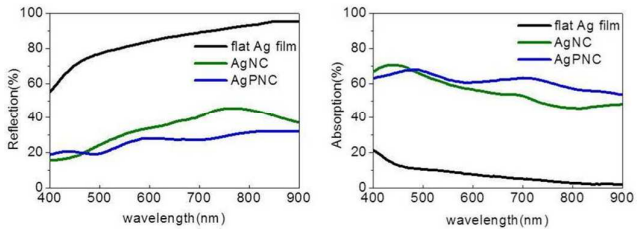

Fig.3 Optical reflection and absorption spectra of flat Ag film, AgNC, AgPNC with Ag thickness=30nm

thick Ag was evaporated on the porous cone by electron beam evaporation with a slow evaporation rate of 0.5 Å/s which enabled the conformal coating of Ag on the polymer nanostructures.

3.2 Structure of SERS substrate

In order to demonstrate the SERS effect of the porosity in metal structure, two types of SERS substrates were fabricated: Ag coated nanocone (AgNC) and Ag coated porous nanocone (AgPNC). Figure 2 shows the SEM images of AgNC and AgPNC. Figure 2a and 2b are 30º-tilt SEM views of the AgNC and AgPNC, respectively. In AgNC, Ag was deposited uniformly on the bottom substrate but small Ag grains were formed on the sidewall of the nanocones. The selective wet etching step was excluded in the fabrication of AgNC substrate, thus the final form of AgNC has no internal porosity. On the other hand, AgPNC has lots of metal nanogaps and protrusions produced at the vacancy of PMMA domain between the cones as well as on the cones. During the nanoimprint, we intentionally left the residual layer of BCP film on the substrate to make porous layer between the cones, and thus to increase the number of SERS hot spots. As shown in the top-view SEM image (Fig. 2c), AgNC arrays are hexagonally arranged over the large area (1 cm ×1.5 cm). Fig. 2d shows the cross-section images of AgNC(upper) and AgPNC(lower) obtained by FIB-SEM. AgNC has solid cone structure with conformal Ag coating, while AgPNC has pores in the polymer with corrugated Ag coating on the surface. An individual polymer cone of AgNC has ~ 300 nm height and ~ 260 nm base diameter. AgPNC has ~200 nm height and ~ 280 nm base diameter. The difference in feature sizes between AgNC and AgPNC is caused by the collapse of nanocone structure because the residual PS domain loses the support of the PMMA block after the selective wet etching step. [31] (See supplementary information Fig. S3)

3.3 Optical properties

In order to understand far-field optical properties of the fabricated structures, we measured reflection and absorption of the flat Ag film, AgNC and AgPNC in wavelength range 400-900 nm by using UV-vis-NIR spectrophotometer (UV3600, Shimadzu Scientific Instruments) with an integrating sphere (MPC-3100). The reflection of AgNC decreases and absorption increases over 40% compared to the flat Ag film in the measured spectrum range. This is due to the antireflective and light absorptive properties of metal-coated conical structures, induced from LSPR.[32, 33] AgPNC shows lower reflection and higher absorption values than those of AgNC because porosity-induced nanogaps and protrusions leads to efficient LSPR excitation. The broad size distribution of the internal nanostructures excites resonant plasmons at various frequencies, and thus leads to broadband light absorption.[34, 35] Broadband LSPR excitation is advantageous in real application because it allows more versatile choice of excitation laser.[36]

3.4 SERS characteristics

To evaluate SERS effect, we measured Raman signal of $10^{-5}M$ R6G on the flat Ag film, AgNC and AgPNC substrates, as shown in Fig. 4. Two different lasers equipped with a Raman microscope were used; 633 nm He-Ne laser for off-resonance excitation and 532 nm ND:YAG laser for on-resonance excitation of R6G. On-resonant excitation induces both SERS effect and resonance Raman effect, while off-resonant excitation induces only SERS effect.[37]

Figure 4 shows the obtained Raman spectra of R6G on the flat Ag film, AgNC and AgPNC under 633 nm (left) and 532 nm (right) excitations, respectively. Under 633 nm excitation (Fig 4a), the flat Ag film shows little Raman signal distinguishable from the noise signal. Raman signal of the AgPNC compared to that of the AgNC is 7.4 times enhanced on average for the R6G peaks at 614, 773, 1182, 1315, 1364, 1512, 1577, 1651 cm^{-1}. Among these peaks, maximum enhancement 8.9 times was obtained at 1315 cm^{-1} peak. This result suggests that internal nanogaps or protrusions in the AgPNC play significant role for SERS enhancement. Strong Raman peaks at 809, 971 and 1284 cm^{-1} were also found which are not related to R6G. These peaks are from the PS-b-PMMA under the Ag layer, which could be detected owing to large SERS enhancement.[38] Under 532 nm excitation, Raman signal of the AgPNC compared to that of the AgNC shows average enhancement 2.6 times. The maximum enhancement 3 times was obtained at 1361cm^{-1}. For both excitation wavelengths, AgPNC shows higher Raman intensity compared with the AgNC. The result indicates that internal nanogaps or protrusions in the AgPNC bring strong near-field enhancement and SERS effect.

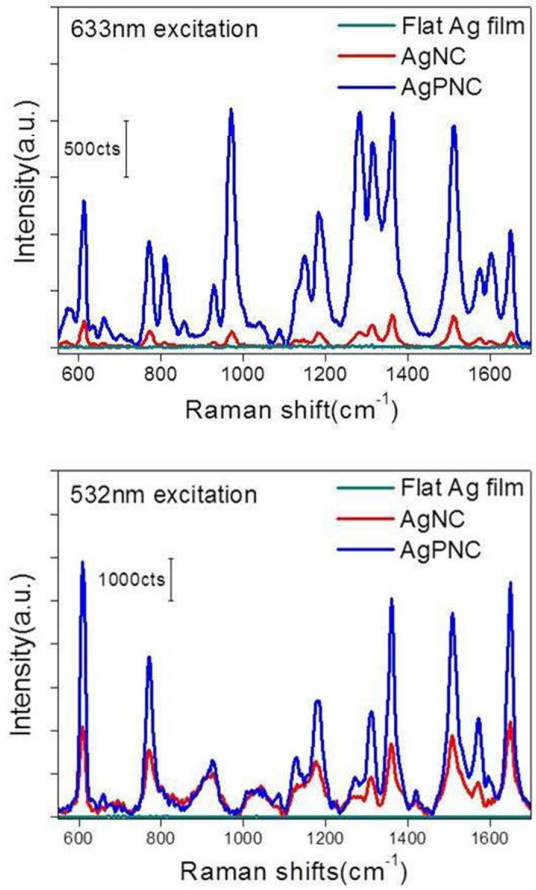

Fig.4 Raman spectra of R6G 10^{-5}M on flat Ag film, AgNC, AgPNC with excitation wavelength of (left) 633nm, (right) 532nm. Each data point represents the averaged SERS spectra from 5 points in the same substrate

More quantitative SERS enhancement factor of AgPNC can be obtained by the analytical enhancement factor (AEF) formula $EF = (I_{SERS}/I_{ref})/(C_{SERS}/C_{ref})$.[39] I_{SERS} and I_{ref} correspond to the Raman intensities of R6G on SERS substrate and glass, respectively. C_{SERS} and C_{ref} denote the molar concentration of R6G in ethanol solution on SERS substrate ($10^{-5}M$) and glass ($10^{-1}M$), respectively. Calculated SERS EF of each R6G Raman band is presented in Table 1.[40] We find that EF reaches up to 7.82×10^4 and 3.47×10^6 under the 633 nm and 532 nm excitations, respectively.

To further investigate the relation between the thickness of Ag coating and the SERS enhancement, we varied the thickness of deposited Ag coating with 30, 50, 70 nm for both AgNC and AgPNC substrates. Let us focus on the AgPNC first. Figure 5 (a)~(c) show the SEM images of AgPNCs with increasing Ag thicknesses. As the thickness of Ag coating increases to 50 nm, internal nanostructures in the polymer matrix are buried under the Ag coating so that the porosity of the AgPNC seems reduced. The corresponding Raman spectra are shown in Figure 5(d) and 5(g) under two different excitations. In this figure, the number after AgPNC refers to the Ag thickness in nm unit.

Table 1. Peak assignment and SERS enhancement factor

	Normal Raman (cm^{-1})	SERS (cm^{-1})	Vibrational Assignment	Enhancement Factor
633nm excitation	612	612	C-C-C ring in plane vibration	6.4×10^4
	772	772	C-H out-of plane bending	5.27×10^4
	1180	1184	C-H in plane bending	5.82×10^4
	1318	1315	N-H in plane bending	7.82×10^4
	1360	1364	arom C-C stretching	7.33×10^4
	1514	1514	arom C-C stretching	5.88×10^4
		1577	N-H in plane bending	
	1649	1651	arom C-C stretching	3.92×10^4
532nm excitation	612	609	C-C-C ring in plane vibration	3.47×10^6
	772	772	C-H out-of plane bending	3.36×10^6
		1179	C-H in plane bending	
		1310	N-H in plane bending	
	1364	1361	arom C-C stretching	2.8×10^6
	1512	1509	arom C-C stretching	1.75×10^6
		1574	N-H in plane bending	
	1650	1650	arom C-C stretching	1.28×10^6

We observe that Raman intensity of the AgPNC30 shows the highest spectra among the 3 samples for both excitation wavelengths. In order for more quantitative comparison, we pay attention to the peak at 1315 cm^{-1}, as shown in Figure 5(e) (under 633 nm excitation) and 5(h) (under 532 nm excitation). AgPNC showed no particular thickness-dependence in the range 30 ~ 70 nm. On the other hand, the Raman intensities of AgNC increase with increasing Ag thickness from 30 nm to 70 nm. These observations indicate that the internal structures such as nanogaps or protrusions play more important roles for Raman spectra enhancement than the effect of Ag thickness. Judging from the experimental results, the optimal Ag film thickness on AgPNC is ~ 30 nm for generating small nanogaps ≤ 10 nm. Because the size of spacing between two adjacent PS ligament before Ag coating is 20 ~ 40 nm, Ag coating thickness above 30 nm reduces the number of metal nanogaps, whereas thinner Ag coating makes large nanogaps > 10 nm which have rather low E-field enhancement. The ratio of Raman intensity between AgPNC and AgNC (I_{AgPNC}/I_{AgNC}) for 30 nm-thick Ag coating reaches up to 8.9 times and 3 times under 633 nm and 532 nm excitation, respectively. For the cases of 70 nm- thick Ag coatings, however, the Raman intensity ratio I_{AgPNC} / I_{AgNC} approaches to ~ 1 indicating that poorer hot spot formation for thicker Ag coatings.

To analyze the local electric field distribution of AgNC and AgPNC with 30nm Ag coating, we performed 2D finite-difference time-domain (FDTD) simulation for the two structures (Lumerical FDTD Solution 8.7.0, Lumerical Inc.,Canada). AgNC was modelled as polystyrene (PS) rounded nanocone with 30nm Ag coating. AgPNC was modeled as Ag coated corrugated polystyrene nanocone and additional corrugation on the bottom substrate. From the SEM images, we observe that the diameter of PS ligament is about 40 nm and that of Ag coated PS ligament is about 60nm. Thus we modelled a "unit corrugation" with a PS cylinder whose radius of curvature is 40 nm and the outer 20 nm Ag shell. On the bottom substrate, the estimated nanogap size between the corrugations is 10 nm. The simulation region is 500 × 2800 nm^2 with a 2 nm uniform mesh at region of -250 nm ≤ x ≤ 250 nm, 0 nm ≤ y ≤ 430 nm and auto non-uniform mesh for the rest of the region.

RSC Advances

ARTICLE

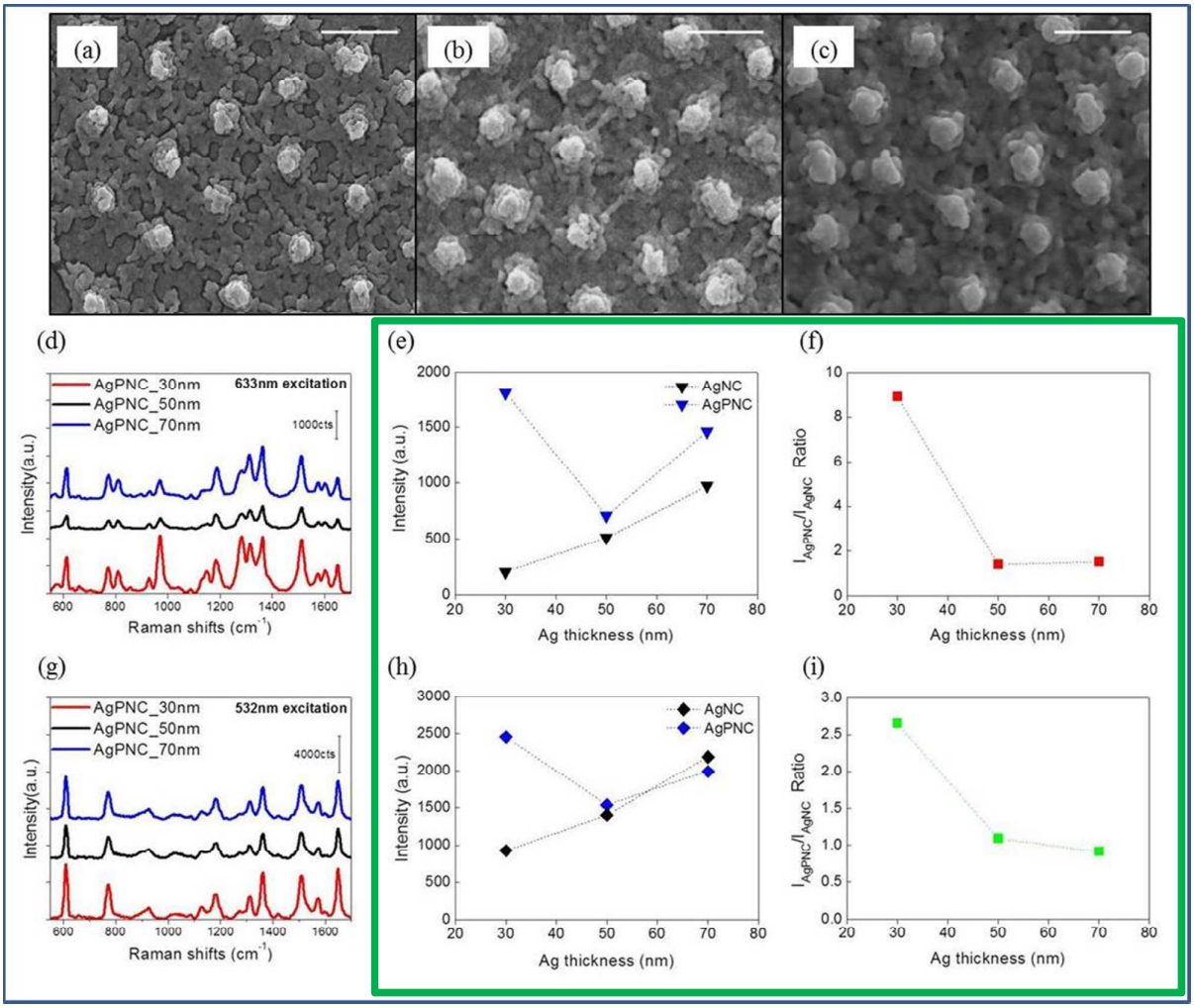

Fig.5 (a-c) SEM images of AgPNC depending on the deposited Ag thickness; (a) 30, (b) 50, (c) 70 nm. White scale bar corresponds to 500 nm. (d,g) SERS spectra of AgPNC with three different Ag thicknesses. (e,h) Effect of Ag thickness on SERS intensity of 1315cm^{-1} R6G peak at (e) 633 nm, (h) 532 nm excitation. (f,i)The intensity ratios of between AgPNC and AgNC at (f) 633 nm, (i) 532 nm excitation.

The boundary condition was set with periodic boundary conditions in x-direction, and a perfectly-matched-layer boundary condition in y-direction. The light source was plane wave propagating along the –y direction with the polarization parallel to the x-axis. The local E-field enhancement $\log|E|^2$, where $|\mathrm{E}| = |\mathrm{E}/E_0|$ (E is the amplitude of local electric field and E_0 is that of incident field), distribution is shown in Fig. 6. For AgNC structure, E-field enhancement from LSPR excitation occurs at the middle of the nanocone at 633 nm excitation, while E-field enhancement appears at the tip and middle of the nanocone at 532 nm. Because the LSPR hotspot is distributed over the large area near the nanocone, E-field enhancement is relatively low. On the other hand, AgPNC structure has multiple strong electric hotspots formed at the nanogaps between the corrugations both for the 633 nm and 532 nm excitations. In particular, stronger hospots are located at the nanocone at 633 nm excitation, whereas hotspots are formed at the bottom substrate at 532nm excitation.

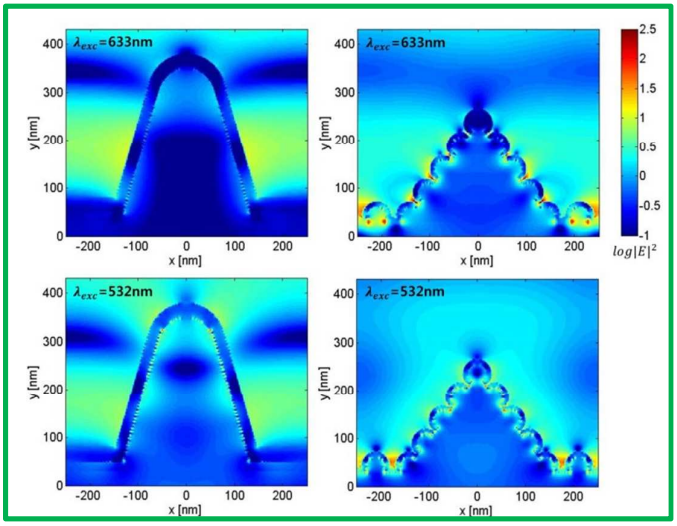

Fig 6. FDTD simulated electric field enhancement of (left column) AgNC and (right column) AgPNC under 633 nm and 532 nm excitation

Regardless of the location, however, the electric field intensity on the surface of AgPNC is always larger than that of AgNC. To sum up the simulation result, porous nanocone has a higher density of stronger electric hotspots compared with solid nanocone, which allows larger SERS enhancement. We calculated theoretical SERS EF by using EF $\approx |E|^4$ approximation and FDTD simulated |E| intensity.[41] Under 633 excitation, the maximum $|E/E_0|$ at the local hot spot of AgPNC structure reaches up to 17.83, which gives theoretical EF $\approx 1.01 \times 10^5$. This EF value corresponds to the experimental maximum EF = 7.82×10^4. For the case of 532 nm excitation, $|E|^4$ approximation is not valid because R6G probe molecules have resonant Raman effect along with SERS effect.

4. Conclusions

In summary, we fabricated porous metallic nanocone arrays with high density electromagnetic hotspots by templating nanoimprinted diblock copolymer with selective etching for SERS application. We introduced solvent-assisted nanoimprint lithography for low-cost, time efficient patterning of block copolymer film into nanocone arrays.

In comparison with solid nanocone, porous nanocone shows maximum 8.9 times enhancement in Raman intensity thanks to the strong near-field enhancement induced from LSPR at nanogaps. The maximum SERS EF is 7.82×10^4 and 3.47×10^6 under the 633 and 532 nm excitation, respectively. By controlling the deposition thickness of Ag coating, we found that sufficiently thin Ag coating (~30 nm) on porous BCP template makes large number of nanogaps and thus bring high SERS enhancement.

Acknowledgements

This research was supported by Basic Science Research Program and the Pioneer Research Center Program through the National Research Foundation of Korea (NRF) funded by the Ministry of Science, ICT and Future Planning (NRF-2015R1A2A2A11001112, NRF-2013M3C1A3065045) and the Low Observable Technology Research Center program of the Defense Acquisition Program Administration and Agency for Defense Development.

References

1. M. G. Albrecht and J. A. Creighton, *Journal of the American Chemical Society*, 1977, **99**, 5215-5217.
2. P. L. Stiles, J. A. Dieringer, N. C. Shah and R. P. Van Duyne, *Annual Review of Analytical Chemistry*, 2008, **1**, 601-626.
3. A. J. Baca, T. T. Truong, L. R. Cambrea, J. M. Montgomery, S. K. Gray, D. Abdula, T. R. Banks, J. Yao, R. G. Nuzzo and J. A. Rogers, *Applied Physics Letters*, 2009, **94**, 243109.
4. T.-H. Lin, N. C. Linn, L. Tarajano, B. Jiang and P. Jiang, *The Journal of Physical Chemistry C*, 2009, **113**, 1367-1372.
5. J. M. Oran, R. J. Hinde, N. Abu Hatab, S. T. Retterer and M. J. Sepaniak, *Journal of Raman Spectroscopy*, 2008, **39**, 1811-1820.
6. A. Kudelski, *Chemical Physics Letters*, 2005, **414**, 271-275.
7. H. Liang, Z. Li, W. Wang, Y. Wu and H. Xu, *Advanced Materials*, 2009, **21**, 4614-4618.
8. H. Im, K. C. Bantz, S. H. Lee, T. W. Johnson, C. L. Haynes and S.-H. Oh, *Advanced Materials*, 2013, **25**, 2678-2685.
9. Y. J. Oh and K. H. Jeong, *Advanced Materials*, 2012, **24**, 2234-2237.
10. Y. Wang, X. Zhao, W. Gao, L. Chen, S. Chen, M. Wei, M. Gao, C. Wang, Y. Zhang and J. Yang, *RSC Advances*, 2015, **5**, 7454-7460.
11. S. Chan, S. Kwon, T. W. Koo, L. P. Lee and A. A. Berlin, *Advanced Materials*, 2003, **15**, 1595-1598.
12. W. Ye, C. Shen, J. Tian, C. Wang, L. Bao and H. Gao, *Electrochemistry Communications*, 2008, **10**, 625-629.
13. Y. Jiao, D. S. Koktysh, N. Phambu and S. M. Weiss, *Applied Physics Letters*, 2010, **97**, 153125.
14. D. Choi, Y. Choi, S. Hong, T. Kang and L. P. Lee, *Small*, 2010, **6**, 1741-1744.
15. M. R. Jones, K. D. Osberg, R. J. Macfarlane, M. R. Langille and C. A. Mirkin, *Chemical Reviews*, 2011, **111**, 3736-3827.
16. L. H. Qian, X. Q. Yan, T. Fujita, A. Inoue and M. W. Chen, *Applied Physics Letters*, 2007, **90**, 153120.
17. J.-S. Wi, S. Tominaka, K. Uosaki and T. Nagao, *Physical Chemistry Chemical Physics*, 2012, **14**, 9131-9136.
18. Y. Jiao, J. D. Ryckman, P. N. Ciesielski, C. A. Escobar, G. K. Jennings and S. M. Weiss, *Nanotechnology*, 2011, **22**, 295302.
19. M. Li, Y. Su, J. Zhao, H. Geng, J. Zhang, L. Zhang, C. Yang and Y. Zhang, *CrystEngComm*, 2015, **17**, 1296-1304.
20. W. Joo, M. S. Park and J. K. Kim, *Langmuir*, 2006, **22**, 7960-7963.
21. D. Zhao, J. Feng, Q. Huo, N. Melosh, G. H. Fredrickson, B. F. Chmelka and G. D. Stucky, *science*, 1998, **279**, 548-552.
22. C. Liang, K. Hong, G. A. Guiochon, J. W. Mays and S. Dai, *Angewandte Chemie International Edition*, 2004, **43**, 5785-5789.
23. G. Kang, J. Yoo, J. Ahn and K. Kim, *Nano Today*, 2015, **10**, 22-47.
24. S. Y. Lee, S.-H. Kim, M. P. Kim, H. C. Jeon, H. Kang, H. J. Kim, B. J. Kim and S.-M. Yang, *Chemistry of Materials*, 2013, **25**, 2421-2426.
25. E. Kim, Y. Xia, X. M. Zhao and G. M. Whitesides, *Advanced Materials*, 1997, **9**, 651-654.

26. S. Claudia, K. Worawut, K. Nikolaos, S. Mathieu, Z. Marc, A. M. Michael and M. S. T. Clivia, *Nanotechnology*, 2014, **25**, 175703.
27. H. Park, D. Shin, G. Kang, S. Baek, K. Kim and W. J. Padilla, *Advanced Materials*, 2011, **23**, 5796-5800.
28. T. W. Odom, J. C. Love, D. B. Wolfe, K. E. Paul and G. M. Whitesides, *Langmuir*, 2002, **18**, 5314-5320.
29. G. Kang, H. Park, D. Shin, S. Baek, M. Choi, D.-H. Yu, K. Kim and W. J. Padilla, *Advanced Materials*, 2013, **25**, 2617-2623.
30. D. Qin, Y. Xia and G. M. Whitesides, *Nature protocols*, 2010, **5**, 491-502.
31. X. Li, L. Xue and Y. Han, *Journal of Materials Chemistry*, 2011, **21**, 5817-5826.
32. M. Toma, G. Loget and R. M. Corn, *Nano letters*, 2013, **13**, 6164-6169.
33. Z. Xu, Y. Chen, M. R. Gartia, J. Jiang and G. L. Liu, *Applied Physics Letters*, 2011, **98**, 241904.
34. Y. Li and Y. Ding, *The Journal of Physical Chemistry C*, 2010, **114**, 3175-3179.
35. M. Bosman, G. R. Anstis, V. J. Keast, J. D. Clarke and M. B. Cortie, *Acs Nano*, 2011, **6**, 319-326.
36. A. D. McFarland, M. A. Young, J. A. Dieringer and R. P. Van Duyne, *The Journal of Physical Chemistry B*, 2005, **109**, 11279-11285.
37. L. Jensen and G. C. Schatz, *The Journal of Physical Chemistry A*, 2006, **110**, 5973-5977.
38. C. De Rosa, F. Auriemma, C. Diletto, R. Di Girolamo, A. Malafronte, P. Morvillo, G. Zito, G. Rusciano, G. Pesce and A. Sasso, *Physical Chemistry Chemical Physics*, 2015, **17**, 8061-8069.
39. E. Le Ru, E. Blackie, M. Meyer and P. G. Etchegoin, *The Journal of Physical Chemistry C*, 2007, **111**, 13794-13803.
40. C.-C. Chang, K.-H. Yang, Y.-C. Liu, C.-C. Yu and Y.-H. Wu, *Analyst*, 2012, **137**, 4943-4950.
41. Z. Dai, F. Mei, X. Xiao, L. Liao, W. Wu, Y. Zhang, J. Ying, L. Wang, F. Ren and C. Jiang, *Nanotechnology*, 2015, **26**, 125603.